Optics & Laser Technology 176 (2024) 110926

Contents lists available at ScienceDirect

Optics and Laser Technology

journal homepage: www.elsevier.com/locate/optlastec

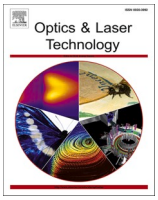

All-fiber-coupled mid-infrared quartz-enhanced photoacoustic sensors

A. Zifarelli [a], R. De Palo [a], S. Venck [b], F. Joulain [b], S. Cozic [b], R. Weih [c], A. Sampaolo [a], P. Patimisco [a,*], V. Spagnolo [a,*]

[a] PolySense Lab, Dipartimento Interateneo di Fisica, University and Politecnico of Bari, Via Amendola 173, 70126 Bari, Italy
[b] Le Verre Fluoré, Brittany, Bruz 35170, France
[c] Nanoplus Nanosystems and Technologies GmbH, Oberer Kirschberg 4, 97218 Gerbrunn, Germany

A B S T R A C T

Infrared laser-based gas sensors are mature to take the leap from laboratory prototype to outdoor operation. Considering the demand of high robustness and compactness, the reliability of the optical alignment in a sensor is the top priority. This paper proposes a solution designing an optical system embedded within a sealed metallic cylinder containing an aspheric micro-lens to couple a single-mode interband cascade laser with an indium fluoride glass fiber. The fiber output is plug & play connected to an acoustic detection module of a quartz-enhanced photoacoustic sensor (QEPAS) equipped with a fiber port, avoiding the use of any free-space optics, from the source to the detection module. To demonstrate the operability, three all-fiber-coupled QEPAS sensors were realized for detection of CH_4, CO_2 and NO reaching sub-ppm ultimate detection limits with a signal integration time of 100 ms.

1 Introduction

The use of fiber delivery in laser-based gas sensing systems offers unmatched advantages: (i) eliminate most of the routine alignment and stability problems; (ii) enable delicate components to be isolated from engine vibration, limiting free-space coupling of sensitive laser sources; (iii) mitigate the ambient interference caused by the CO_2 or water absorption along the free-space optical path. Until now, numerous efforts have been made to directly connect a laser to a gas cell, primarily utilizing laser diodes that are coupled with fibers[1–3]. The most notable detection limits have been reported with sensing systems based on cavity ring-down spectroscopy (CRDS) and photo-acoustic spectroscopy (PAS). The two approaches exploit the light-molecule interaction in two opposite ways: one relying on resonant cavities and thus on direct detection of absorbed light[4], and one relying on the detection of the deposited energy within the sample thus measuring the absorbed light in an indirect way[5]. He et al.[6] proposed a remote fiber-coupled CRDS-based optical sensor for ammonia detection in nitrogen, achieving a measurement deviation (in terms of absorbance) of $\sim 5.4 \times 10^{-9}$ cm^{-1}. Although a high sensitivity is provided, CRDS requires high-quality mirrors and precise optical alignment to achieve the best measurement performance. Bauer et al.[7] demonstrated detection of acetylene in nitrogen with a low-cost 3D-printed PAS sensor, while Cao et al.[8] demonstrated an all-optical PAS sensor for acetylene detection. Even though these are promising advancements in low-cost PAS sensor solutions, the fragility of the diaphragm, the sensitivity to external acoustic and the vibrational noise limits the compatibility with outdoor detection of air pollutants.

In mid-infrared region, the situation is more stagnant. Interband Cascade Lasers (ICLs) and Quantum Cascade Lasers (QCLs) are very promising mid-infrared light sources for gas sensing spectroscopy, mainly operating in the range 3 – 6 μm and 5 – 12 μm, respectively, that take advantage of iterative injected electrons in serially cascaded active regions[9,10]. Moreover, the low power consumption makes ICLs very attractive for battery-operated applications, an added value for the design of sensing systems for outdoor operations[11–13]. Unfortunately, in these spectral ranges, specialty fibers (e.g., germanium oxide, chalcogenide and sapphire) suffer from many limitations, including lower mechanical and chemical properties with respect to silica fibers, high cost, high losses, poor flexibility, and poor biocompatibility, thereby limiting their widespread use[14]. While chalcogenide fibers offer the widest transmission range (up to 20 μm in case of tellurium TeX glasses[15]), Indium Fluoride Glasses (IFG) provide the highest transparency from 2 μm up to 5 μm with background losses < 15 dB/km in the spectral range 2.55 μm-3.55 μm and high transmission from visible up to 5.3 μm (with losses of 1 dB/m)[16]. Moreover, fluoride glasses exhibit relatively low refractive indices (around 1.5) compared to other glasses suitable for mid-IR region. As a result, the Fresnel losses of the fluoride fibers are limited below 4 % and their impact on coupling efficiency and stability is strongly reduced. For these reasons, IFG optical fibers are excellent candidates for pigtailing ICL sources from 2.6 μm up to 5.3 μm [17].

* Corresponding authors.
E-mail addresses: pietro.patimisco@uniba.it (P. Patimisco), vincenzoluigi.spagnolo@poliba.it (V. Spagnolo).

https://doi.org/10.1016/j.optlastec.2024.110926
Received 22 November 2023; Received in revised form 8 March 2024; Accepted 27 March 2024
Available online 4 April 2024

Hollow core fibers, constituting another category of optical fibers designed for mid-IR operation, display distinct advantages. Unlike their solid-core counterparts, these fibers, crafted from a hollow glass capillary tube, are more robust and lack cladding modes. Subsequently, the light is directed within a hollow core, typically ranging from 300 to 800 μm in diameter. Remarkably, despite the substantial core diameter, these fibers exhibit single-mode transmission[18]. Extensive exploration into the transmission characteristics of hollow core fibers for ICL and QCL radiation has been conducted, losses as low as 0.44 dB/m in the 9–10 μm wavelength range has been achieved[19]. The coupling of the laser beam with the HCW entrance is realized by a free-space, aspheric lens. The main drawback is that the single mode beam quality and losses at the fiber output are strongly dependent on the optical coupling at the waveguide entrance, compromising the robustness and mechanical stability of the coupling itself. Utilizing a hollow-core fiber-coupled QCL, Spagnolo et al. conducted highly sensitive spectroscopic measurements of SF_6. The normalized noise-equivalent absorption was determined to be 2.7×10^{-10} W·cm^{-}1/Hz$^{1/2}$. This investigation employed the quartz-enhanced photoacoustic spectroscopy (QEPAS) technique[20].

QEPAS is a variant of PAS where the microphone is replaced by a spectrophone to detect sound waves produced by the absorbing gas via photoacoustic effect[21,22] and this technique has already demonstrated its capability to detect the selected analytes employing traditional free-space optics[23–25]. In QEPAS, the spectrophone is composed by a quartz tuning fork acoustically coupled with a pair of resonator tube, in an on-beam configuration[26]. The optical alignment of a QEPAS sensor strictly requires that the laser beam passes through two resonator tubes and in the gap between the QTF prongs without illuminating them. Collimators, aspheric lenses, and other spatial filtering mechanics are usually employed to avoid touching any surfaces without introducing spherical aberration and preventing diffraction-limited performance. Although the optical alignment is not as critical as cavity-based techniques, the use of free-space optics makes the ultimate performance as well as the long-term stability of a QEPAS sensor extremely susceptible to external vibrations, requiring periodic re-alignment procedures for restoring the initial conditions.

In this work, we report on a QEPAS sensor architecture packaged for portable field operation with no re-alignment requirements. To increase the mechanical rigidity of the coupling arrangement, no free-space optics were used for the entire QEPAS sensor assembly. A single-mode IFG fiber was used to guide the excitation laser into the spectrophone without any other free-space optics. The all-fiber-coupled QEPAS sensor combines the advantages of a sensitive detection based on QEPAS spectroscopy with the flexibility offered by a fiber-coupled systems. The rigid fixation of the fiber to the acoustic detection module (ADM) ensures a high stability of the light excitation beam even if the ADM is moved. The versatility of the developed system is here demonstrated employing three fiber-coupled mid-IR ICLs targeting methane (CH_4), carbon dioxide (CO_2), and nitric oxide (NO), respectively.

2. Fiber coupling of ICL sources

Three free-space emitting ICLs supplied by nanoplus GmbH were selected for fiber coupling operations employing the IFG fibers. The laser sources were characterized by central emission wavelengths of 3.345 μm, 4.230 μm, and 5.263 μm to target CH_4, CO_2, and NO, respectively. The ICLs were provided with an aspheric lens to collimate the beam (f_{coll} = 4 mm), with beam diameters reported in Table 1. A chalcogenide BL-2 glass aspheric lens (f_{chalc} = 5.95 mm, NA_{chalc} = 0.56) with antireflection coating in 3–5 μm range was used to focus the laser beam into the core of the IFG fiber. The beam diameters on the lens focal plane were calculated and are reported in Table 1. IFG optical fibers developed by Le Verre Fluoré were selected to couple the ICL sources[27]. The optical fibers were characterized by NA_{fiber} = 0.30, core diameter of 8.5 μm and 9.5 μm, cladding diameter of 125 μm, with a length of 30 cm. The input mode field diameters (MFDs) for the employed optical fibers were calculated using the Marcuse formula for the mode diameter of a step-index single-mode fiber[28], and the results are reported in Table 1.

The IFG fibers were equipped with FC/APC connectors at the input, which were tilted to avoid etalon effect with the chalcogenide lens, and FC/PC connector at the output. The FC/APC connector was glued on a lens tube which housed the focusing lens, and the system was glued to the laser output embedding the ICL collimating lens. A schematic of the coupling system employed for the ICL sources is shown in Fig. 1a, while in Fig. 1b a photo of the developed fiber-coupled ICL source is reported.

The fiber-coupled ICLs were characterized in terms of total loss, calculated by comparing the output power of the bare ICL and the optical power at the fiber exit, in dB unit. The L-I curves collected before and after the fiber coupling are shown in Fig. 2. The ICL sources emitting at 3.345 μm and 4.230 μm were characterized at an operating temperature of 20 °C, while the ICL source emitting at 5.263 μm was characterized at 10 °C.

The weak drops in the L-I curves of the device 3166/07–30 (λ = 4.230 μm) correspond to CO_2 absorption in air along the small path-length (few centimeters) separating the beam exit and the power meter. As representative, the fiber-coupling total losses are calculated at 110 mA and reported in Table 2.

The total losses are mainly due to the coupling efficiency between the laser source and the fiber entrance, and propagation losses. With a fiber length of 30 cm and theoretical propagation losses estimated in the order of several dB/km, these kinds of losses can be neglected. Losses in optical coupling include contributions due to: i) the absorption related to the chalcogenide lens (~15 % absorption in the operating wavelength range estimated for the 2.5 mm thick BL-2, as reported by the

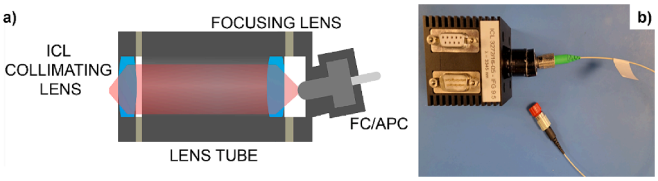

Fig. 1. (a) Schematic of the coupling system employed. (b) Photo of the IFG fiber-coupled ICL 3272/16–05. The green input FC/APC connector is glued to the metallic cylinder, while the black output FC/PC connector is protected by a red cap.

Table 1
ICL sources and fibers employed for optical coupling. Beam profile parameters of the ICL sources are reported in the table, as well as the characteristics of the selected IFG fibers.

ICL serial number	ICL $\lambda_{emission}$ (μm)	Output beam diameter (mm)	Calculated focused beam diameters (μm)	IFG fiber model	Core diameter (μm)	Fiber MFD at λ_{ICL} (μm)
3272/16–05	3.345	4.31 × 3.98	4.0 × 4.3	IFG SM 9.5/125	9.5	9.8
3166/07–30	4.230	3.72 × 3.92	5.8 × 5.5	IFG SM 8.5/125	8.5	11.3
3634/01–01	5.263	5.40 × 4.31	5.0 × 6.2	IFG SM 9.5/125	9.5	14.2

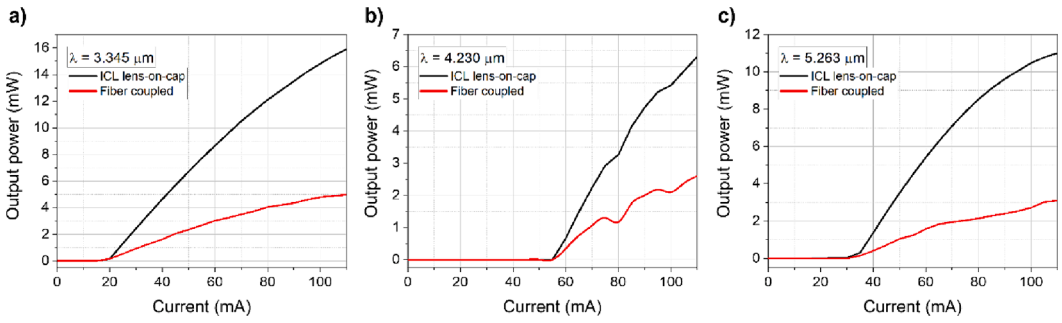

Fig. 2. Measured output power as a function of ICL operating current for the employed devices: (a) 3272/16–05 (λ = 3.345 μm); (b) 3166/07–30 (λ = 4.230 μm); (c) 3634/01–01 (λ = 5.263 μm). Optical powers were measured at the output of the ICL lens on cap and at the output of fiber-coupled ICL.

Table 2
Optical powers at the ICL exit and at the fiber exit, measured with an injected current of 110 mA for the three investigated ICLs. The total losses are estimated in dB unit.

ICL serial number	ICL $\lambda_{emission}$ (μm)	Output power at the ICL exit, at 110 mA (mW)	Output power at the fiber exit at 110 mA (mW)	Total Loss (dB)
3272/16–05	3.345	15.9	5.0	5.1
3166/07–30	4.230	6.3	2.6	3.8
3634/01–01	5.263	11.0	3.1	5.5

manufacturer); ii) the mode field diameter differences and ICL mode ellipticity reported in Table I; (iii) slight misalignments of the optical fiber in gluing mechanical procedure. The Fresnel reflection ascribed to the chalcogenide lens (refractive index of 2.3) is below 1.5 % due to the antireflective coating and thus can be neglected.

The spatial beam profiles at the IFG fibers exit were acquired using an infrared pyrocamera (Ophir Spiricon III) with a spatial resolution of 100 μm. The intensity distributions of the three ICLs operating at 100 mA are shown in Fig. 3 with the pyrocamera placed ~ 2 cm far from the fiber exit, as representative.

The intensity distribution profiles exhibit a symmetric, Gaussian-like beam shape, as also observed in the whole current dynamic range of the three fiber-coupled ICLs. Half-angle beam divergences of the beams were calculated by extracting the beam widths from the beam profiles acquired by placing the pyrocamera at different distances from the fiber exit[29]. In all investigated cases, the angular divergence falls in the range 70–80 mrad.

3. Fiber-Coupled acoustic detection module

The core of any QEPAS sensor is the ADM. It contains the spectrophone enclosed in a stainless-steel housing with inlet and outlet connectors for gas flowing, and two windows for laser beam entrance and exit. A commercial ADM has been provided by Thorlabs GmbH (ADM01), with a spectrophone consisting of a T-shaped QTF acoustically coupled with a pair of resonator tubes, showing a resonance frequency f_o = 12456.1 Hz. The geometry and sizes of the ADM01 are reported in Ref.[30]. A detailed investigation of the influence of the air pressure on the resonance properties of the spectrophone mounted in the ADM01 was studied in Ref.[31]. The fiber-coupled ADM was developed implementing a compact, ultra-stable fiber port (THORLABS PAF2-4E) integrated in the ADM01 and equipped with micro-positioners to provide an easy-to-use platform for coupling light out of optical fibers. The sketch of the designed fiber-coupled ADM is shown in Fig. 4.

The main guidelines for the design have been compact size, high-resolution alignment mechanism, high thermal stability and translation locking mechanisms. The fiber port includes an aspheric lens with an effective focal length of 4 mm and an anti-reflection coating in the spectral range 2–5 μm. It was realized with FC/PC, fiber bulkheads. A detailed description of the alignment procedure for the fiber port is reported in the Thorlabs website[32]. As a result, the 5-axis adjustment

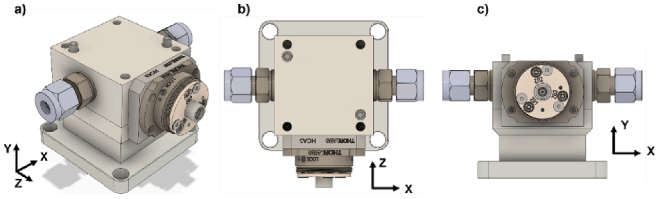

Fig. 4. CAD drawings of the developed fiber-coupled ADM: (a) 3D view; (b) top view; (c) front view.

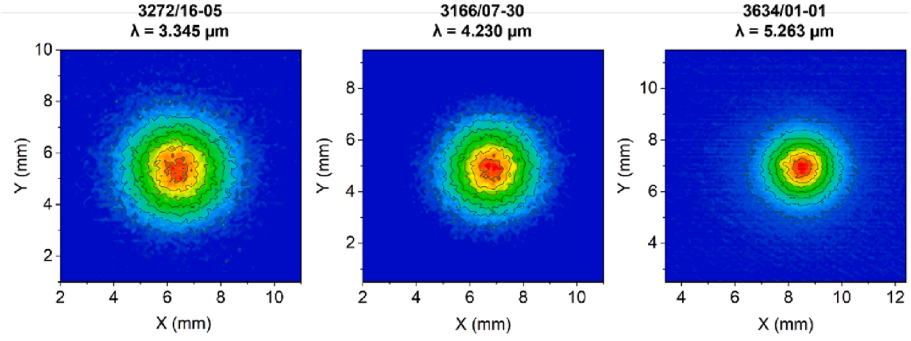

Fig. 3. Beam profiles acquired at the output of the optical fibers operating the ICL sources at I = 100 mA. Color scale is normalized to the peak intensity of each beam spot.

combined with their short focal length leads to negligible off-axis sensitivity.

4. All-Fiber-coupled QEPAS sensors

The fiber-coupled ADM has been combined with three fiber-coupled ICLs to develop the first all-fiber-coupled QEPAS sensors without free-space optics. A sketch of the employed experimental setup and two representative pictures of an all-fiber-coupled QEPAS sensor are reported in Fig. 5.

The main advantages expected with respect to the standard QEPAS sensor with free-space optics are: (i) open optical path reduced to few millimeters; (ii) optic-less, plug & play fiber connectors; (iii) ultimate sensitivity not affected by open-air absorption.

The fiber-coupled ADM was tested with the three fiber-coupled ICLs described in the previous section assembled to realize three all fiber-coupled QEPAS sensors for the detection of CH_4, CO_2 and NO, respectively. The fiber-coupled configuration allowed an easy switching among the ICL sources, without the need for further alignment adjustments. The CH_4 QEPAS sensor targets the methane absorption line peaked at 2988.8 cm^{-1}; the CO_2 QEPAS sensor is tuned on the carbon dioxide strong absorption feature at 2361.5 cm^{-1}; and the NO QEPAS sensor targets the isolated nitric oxide absorption line at 1900.0 cm^{-1}[33]. To reach these wavelengths, the ICLs were operated at T = 30 °C, T = 5 °C, and T = 6 °C, respectively.

For all three cases, QEPAS measurements were executed exploiting a wavelength modulation (WM) configuration. In this process, a sinusoidal modulation at $f_0/2$ was applied to the ICL current driver (THORLABS ITC4002QCL). Simultaneously, the electrical signal generated by the spectrophone underwent demodulation by the lock-in amplifier (Zurich Instruments MFIA 500 kHz Lock-in Amplifier) at f_0. For all measurements reported in this work, the lock-in time constant was set at 100 ms and the sampling time set at three times the lock-in time constant.

A pressure controller (MKS Type 649) was used to fix the gas mixture's pressure in the fiber-coupled ADM, and the flow rate was regulated using a gas mixer (MCQ Instruments, Gas Blender 103). To introduce humidity into the gas samples, a Nafion humidifier (Perm-Select PDMSXA 1 cm^2) was positioned after the gas mixer, maintaining a consistent water vapor concentration of 1 % throughout all measurements. The CH_4 and NO QEPAS sensors operate at a pressure of 250 Torr, while the optimal pressure for CO_2 sensor was set to 760 Torr. For all three QEPAS sensor, the gas flow rate was fixed at 50 sccm.

The CH_4 sensor was calibrated by mixing a certified concentration of 9.9 ppm CH_4:N_2 with pure N_2 down to 2.0 ppm; the CO_2 sensor by mixing a certified concentration of 1000 ppm CO_2:N_2 with pure N_2 down to 200 ppm; the NO sensor starting from a certified concentration of 10.9 ppm NO:N_2, down to 5.4 ppm when diluted in pure N_2. For all three QEPAS sensors, starting from the certified concentrations, QEPAS

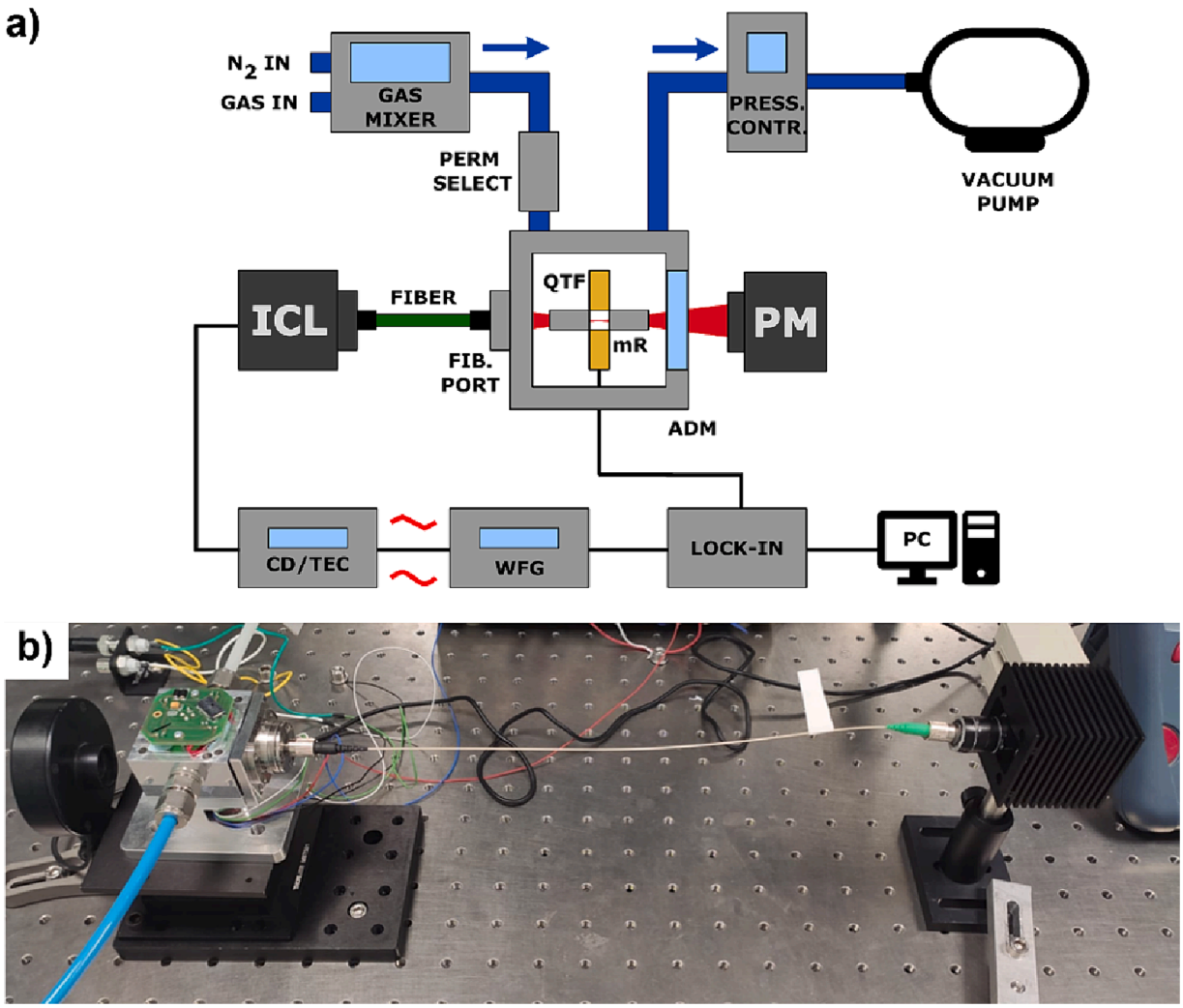

Fig. 5. A) sketch of the employed experimental setup: waveform generator (wfg), micro-resonators tubes (mr). b) photo of the developed all-fiber-coupled qepas sensor, including the adm equipped with the fiber port (left) and the fiber-coupled icl source (right). the optical fiber connecting the two sensor elements is also visible.

spectral scans of the selected absorption feature were acquired at different dilutions. The measured QEPAS spectral scans for CH_4, CO_2 and NO are shown in Fig. 6a, b and c, respectively.

For each spectral scan, peak values were extracted and plotted as a function of the analyte concentration to evaluate the sensor's response. The results are reported in Fig. 7a, b and c together with their best linear fit.

The sensor's sensitivity was estimated starting from the slope retrieved by the best linear fit, while for each sensor the minimum detection limit (MDL) was calculated as the concentration providing a signal-to-noise ratio equal to 1. The sensors' sensitivities, the measured noise levels, and the calculated MDLs are reported in Table 3. The noise level, and thus the ultimate detection limit, can be further improved by increasing the signal integration time. The Allan-Werle deviation analysis is the most common method largely employed in spectroscopy techniques, providing, directly, the noise-vs-integration time (τ) trend in the form of a log–log deviation[34]. Data plot allows the different noise and drift types to be readily identified by the slopes of the different plot regions. The Allan-Werle deviation analysis acquired for the CO_2 sensor is shown in Fig. 8, as representative.

The Allan-Werle deviation analysis for CH_4 and NO fiber-coupled QEPAS sensors follows the same trend as that one showed for the CO_2 QEPAS sensor. The Allan deviation analysis shows that for integration times < 10 s the QEPAS noise level follows the $1/\sqrt{\tau}$ trend, demonstrating that the QTF thermal noise is the dominant noise source. At $\tau >$ 10 s, the noise level remains quite flat: this is in contrast with trends observed in standard QEPAS sensors, where a turnover point usually appears, beyond that the noise level starts to deteriorate. The turnover point indicates the occurrence of other long-term effects, which overwhelm the QTF thermal noise, mainly ascribed to mechanical instabilities. For all-fiber-coupled QEPAS sensors the absence of a turnover point clearly indicates the improvement of the mechanical stability of the sensing system for long-term operations. By means of the Allan-Werle deviation analysis, it is possible to estimate the MDL at longer integration time, thus the MDL evaluated at 10 sec of integration time was selected as ultimate detection limit for the sensors and reported in Table 3.

The achieved results demonstrate the possibility to reach sub-ppm sensitivities for the three developed fiber-coupled QEPAS sensors, both operating in real time ($\tau = 0.1$ s) and at longer integration time ($\tau = 10$ s).

5. Conclusions

In this work, the development of an all-fiber-coupled mid-IR QEPAS sensor was reported. With this aim, three mid-IR ICL sources targeting absorption features of CH_4, CO_2, and NO, were fiber-coupled using IFG optical fibers with good coupling performances and single-mode transmission. The measured total losses were 5.1 dB, 3.8 dB, and 5.5 dB for the devices emitting at 3.345 μm, 4.230 μm, and 5263 μm, respectively.

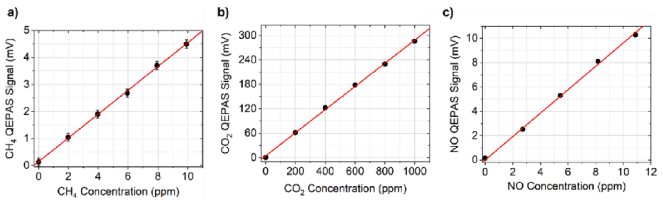

Fig. 7. QEPAS peak signals as a function of the gas target concentration (black dots) and corresponding best linear fit (red solid line) for (a) CH_4, (b) CO_2, and (c) NO, respectively. Error bars are calculated from the measured fluctuations of peak signals over time.

Table 3
Summary of the performances for the detection of three analytes with all-fiber-coupled QEPAS sensor.

	CH_4 QEPAS Sensor	CO_2 QEPAS Sensor	NO QEPAS Sensor
Sensitivity	0.45 mV/ppm	0.28 mV/ppm	0.95 mV/ppm
Noise Level	0.135 mV	0.127 mV	0.160 mV
MDL at 0.1 sec	300 ppb	440 ppb	170 ppb
MDL at 10 sec	80 ppb	115 ppb	50 ppb

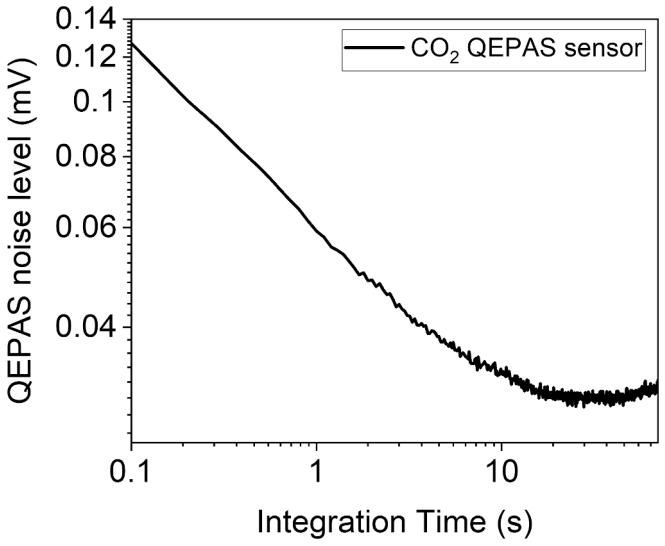

Fig. 8. Results of Allan-Werle Deviation Analysis performed on the CO_2 QEPAS sensor.

The output of the fiber-coupled lasers was directly focused into a custom ADM equipped with a fiber port with fine alignment mechanism. No additional free-space optics were needed in the developed system, thus

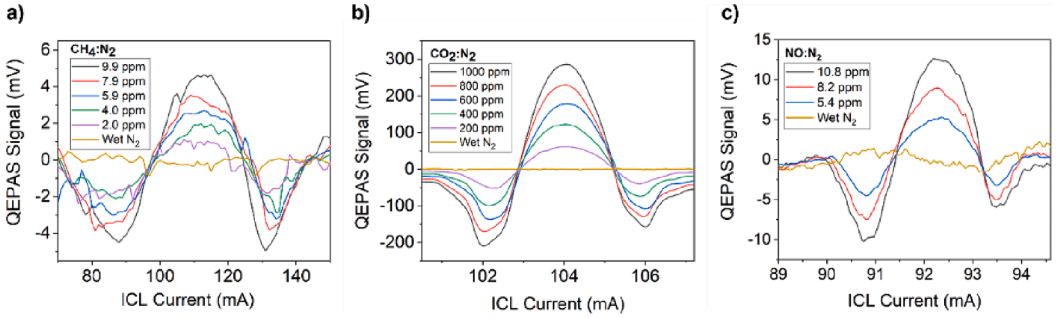

Fig. 6. *2f*-QEPAS spectral scans acquired diluting the certified concentrations of target gases in humidified N_2: (a) CH_4 diluted from 9.9 ppm, (b) CO_2 diluted from 1000 ppm, and (c) NO diluted from 10.8 ppm, in N_2.

resulting in a compact and rugged the gas sensor. The versatility and the wavelength independence characteristic of QEPAS technique could be fully exploited since it was possible to switch the three fiber-coupled sources without any further adjustment. Indeed, the three selected analytes were targeted employing a single ADM. The QEPAS sensor was calibrated for each gas target demonstrating linear responses and sub-ppm detection limits when operated in real time ($\tau = 0.1$ s). The achieved concentrations are below natural abundance of the selected analytes. Therefore, the developed fiber-coupled sensor represents a solid candidate for on field, environmental monitoring, with the next step involving the transfer of this technology outside of laboratory, to develop sensing platforms capable to be operated on mobile vehicle and also on-drone.

Funding

All authors acknowledge funding from the European Union's Horizon 2020 research and innovation program under grant agreement No. 101,016,956 PASSEPARTOUT, in the context of the Photonics Public Private Partnership. Authors from PolySensSe Lab acknowledge also funding from PNRR MUR project PE0000023-NQSTI; MUR – Dipartimenti di Eccellenza 2023–2027 – Quantum Sensing and Modelling for One-Health (QuaSiModO).

CRediT authorship contribution statement

A. Zifarelli: Writing – original draft, Investigation, Data curation, Conceptualization. **R. De Palo:** Writing – original draft, Investigation, Data curation. **S. Venck:** Writing – review & editing, Investigation. **F. Joulain:** Writing – review & editing, Data curation. **S. Cozic:** Writing – review & editing, Data curation. **R. Weih:** Writing – review & editing, Conceptualization. **A. Sampaolo:** Writing – review & editing, Data curation, Conceptualization. **P. Patimisco:** Writing – review & editing, Writing – original draft, Formal analysis, Data curation, Conceptualization. **V. Spagnolo:** Writing – review & editing, Supervision, Funding acquisition, Conceptualization.

Declaration of competing interest

The authors declare that they have no known competing financial interests or personal relationships that could have appeared to influence the work reported in this paper.

Data availability

Data will be made available on request.

References

[1] R. Cui, L. Dong, H. Wu, W. Ma, L. Xiao, S. Jia, W. Chen, F.K. Tittel, Three-dimensional printed miniature fiber-coupled multipass cells with dense spot patterns for ppb-level methane detection using a Near-IR diode laser, Anal. Chem. 92 (2020) 13034–13041.
[2] K. Liu, L. Wang, T. Tan, G. Wang, W. Zhang, W. Chen, X. Gao, Highly sensitive detection of methane by near-infrared laser absorption spectroscopy using a compact dense-pattern multipass cell, Sensors Actuators b. Chem. 220 (2015) 1000–1005.
[3] W. Duan, F. Yan, Y. Wang, H. Zhang, L. Ma, D. Wen, W. Wang, G. Sheng, Q. Wang, A laser-based multipass absorption sensor for sub-ppm detection of methane, Acetylene and Ammonia, Sensors. 22 (2022) 556.
[4] A. Maity, S. Maithani, M. Pradhan, Cavity ring-down spectroscopy: Recent technological advances and applications, in: Mol. Laser Spectrosc. Adv. Appl. Vol. 2, American Chemical Society, 2020: pp. 83–120.
[5] M. Bertolotti, R. Li voti, A note on the history of photoacoustic, thermal lensing, and photothermal deflection techniques, J. Appl. Phys. 128 (2020) 230901.
[6] Y. He, C. Jin, R. Kan, J. Liu, W. Liu, J. Hill, I.M. Jamie, B.J. Orr, Remote open-path cavity-ringdown spectroscopic sensing of trace gases in air, based on distributed passive sensors linked by km-long optical fibers, Opt. Express. 22 (2014) 13170.
[7] R. Bauer, G. Stewart, W. Johnstone, E. Boyd, M. Lengden, 3D-printed miniature gas cell for photoacoustic spectroscopy of trace gases, Opt. Lett. 39 (2014) 4796.
[8] Y. Cao, W. Jin, H.L. Ho, J. Ma, Miniature fiber-tip photoacoustic spectrometer for trace gas detection, Opt. Lett. 38 (2013) 434.
[9] J. Meyer, W. Bewley, C. Canedy, C. Kim, M. Kim, C. Merritt, I. Vurgaftman, The interband Cascade laser, Photonics. 7 (2020) 75.
[10] M. Pal, M. Pradhan, Quantum Cascade Laser Spectroscopy, in: Springer, Singapore, 2021: pp. 363–387.
[11] C.R. Webster, P.R. Mahaffy, S.K. Atreya, J.E. Moores, G.J. Flesch, C. Malespin, C. P. McKay, G. Martinez, C.L. Smith, J. Martin-Torres, J. Gomez-Elvira, M. P. Zorzano, M.H. Wong, M.G. Trainer, A. Steele, D. Archer, B. Sutter, P.J. Coll, C. Freissinet, P.Y. Meslin, R.V. Gough, C.H. House, A. Pavlov, J.L. Eigenbrode, D. P. Glavin, J.C. Pearson, D. Keymeulen, L.E. Christensen, S.P. Schwenzer, R. Navarro-Gonzalez, J. Pla-García, S.C.R. Rafkin, Á. Vicente-Retortillo, H. Kahanpää, D. Viudez-Moreiras, M.D. Smith, A.M. Harri, M. Genzer, D. M. Hassler, M. Lemmon, J. Crisp, S.P. Sander, R.W. Zurek, A.R. Vasavada, Background levels of methane in Mars' atmosphere show strong seasonal variations, science (80-,) 360 (2018) 1093–1096.
[12] J. Hillbrand, M. Beiser, A.M. Andrews, H. Detz, A. Schade, R. Weih, S. Höfling, B. Schwarz, G. Strasser, Monolithic frequency comb platform based on interband cascade lasers and detectors, Opt. Vol. 6, Issue 7, Pp. 890-895. 6 (2019) 890–895.
[13] L. Dong, C. Li, N.P. Sanchez, A.K. Gluszek, R.J. Griffin, F.K. Tittel, Compact CH4 sensor system based on a continuous-wave, low power consumption, room temperature interband cascade laser, Appl. Phys. Lett. 108 (2016) 11106.
[14] G. Tao, H. Ebendorff-Heidepriem, A.M. Stolyarov, S. Danto, J.V. Badding, Y. Fink, J. Ballato, A.F. Abouraddy, Infrared fibers, Adv. Opt. Photonics. 7 (2015) 379.
[15] J. Lucas, X.H. Zhang, The tellurium halide glasses, J. Non. Cryst. Solids. 125 (1990) 1–16.
[16] J.-P. Yehouessi, S. Vidal, J.-Y. Carree, L. Bodin, S. Cozic, T. Berthelot, S. Poulain, L. Calvez, G. Huss, J. Boullet, 3 W Mid-IR supercontinuum extended up to 4.6 μm based on an all-PM thulium doped fiber gain-switch laser seeding an InF3 fiber, in: P.G. Schunemann, K.L. Schepler (Eds.), Nonlinear Freq. Gener. Convers. Mater. Devices XVIII, SPIE, 2019: p. 6.
[17] A. Annunziato, F. Anelli, P.L.P. Du Teilleul, S. Cozic, S. Poulain, F. Prudenzano, Fused optical fiber combiner based on indium fluoride glass: perspectives for mid-IR applications, Opt. Express. 30 (2022) 44160.
[18] J.M. Kriesel, N. Gat, B.E. Bernacki, R.L. Erikson, B.D. Cannon, T.L. Myers, C.M. Bledt, J.A. Harrington, Hollow core fiber optics for mid-wave and long-wave infrared spectroscopy, in: Chem. Biol. Radiol. Nucl. Explos. Sens. XII, SPIE, 2011: p. 80180V.
[19] M. Giglio, P. Patimisco, A. Sampaolo, J.M. Kriesel, F.K. Tittel, V. Spagnolo, Low-loss and single-mode tapered hollow-core waveguides optically coupled with interband and quantum cascade lasers, Opt. Eng. 57 (2018) 1.
[20] V. Spagnolo, P. Patimisco, S. Borri, G. Scamarcio, B.E. Bernacki, J. Kriesel, Part-per-trillion level SF_6 detection using a quartz enhanced photoacoustic spectroscopy-based sensor with single-mode fiber-coupled quantum cascade laser excitation, Opt. Lett. 37 (2012) 4461–4463.
[21] A.A. Kosterev, Y.A. Bakhirkin, R.F. Curl, F.K. Tittel, Quartz-enhanced photoacoustic spectroscopy, Opt. Lett. 27 (2002) 1902.
[22] Y. Ma, Review of recent advances in QEPAS-based Trace gas sensing, Appl. Sci. 8 (2018) 1822.
[23] G. Menduni, A. Zifarelli, E. Kniazeva, S. Dello Russo, A.C. Ranieri, E. Ranieri, P. Patimisco, A. Sampaolo, M. Giglio, F. Manassero, E. Dinuccio, G. Provolo, H. Wu, D. Lei, V. Spagnolo, Measurement of methane, nitrous oxide and ammonia in atmosphere with a compact quartz-enhanced photoacoustic sensor, Sensors Actuators B Chem. 375 (2023) 132953.
[24] Y. Liu, H. Lin, B.A.Z. Montano, W. Zhu, Y. Zhong, R. Kan, B. Yuan, J. Yu, M. Shao, H. Zheng, Integrated near-infrared QEPAS sensor based on a 28 kHz quartz tuning fork for online monitoring of CO2 in the greenhouse, Photoacoustics. 25 (2022) 100332.
[25] C. Shi, D. Wang, Z. Wang, L. Ma, Q. Wang, K. Xu, S.C. Chen, W. Ren, A mid-Infrared fiber-coupled QEPAS nitric oxide sensor for real-time engine exhaust monitoring, IEEE Sens. J. 17 (2017) 7418–7424.
[26] P. Patimisco, A. Sampaolo, L. Dong, F.K. Tittel, V. Spagnolo, Recent advances in quartz enhanced photoacoustic sensing, Appl. Phys. Rev. 5 (2018) 011106.
[27] Le Verre Fluoré - IFG Single Mode - https://leverrefluore.com/products/passive-fibers/ifg-single-mode, (n.d.).
[28] D. Marcuse, Loss analysis of single-mode fiber splices, Bell Syst. Tech. J. 56 (1977) 703–718.
[29] P. Patimisco, V. Spagnolo, M.S. Vitiello, G. Scamarcio, C.M. Bledt, J.A. Harrington, Low-Loss Hollow Waveguide Fibers for Mid-Infrared Quantum Cascade Laser Sensing Applications, Sensors 2013, Vol. 13, Pages 1329-1340. 13 (2013) 1329–1340.
[30] R. De Palo, A. Elefante, G. Biagi, F. Paciolla, R. Weih, V. Villada, A. Zifarelli, M. Giglio, A. Sampaolo, V. Spagnolo, P. Patimisco, Quartz-enhanced photoacoustic sensors for detection of eight air pollutants, Adv. Photonics Res. 4 (2023).
[31] M. Olivieri, A. Zifarelli, G. Menduni, M. Di Gioia, C. Marzocca, V.M.N. Passaro, A. Sampaolo, M. Giglio, V. Spagnolo, P. Patimisco, Influence of air pressure on the resonance properties of a t-shaped quartz tuning fork coupled with resonator tubes, Appl. Sci. 11 (2021) 7974.

[32] THORLABS ADM01 https://www.thorlabs.com/newgrouppage9.cfm?objectgroup_id=2940, (n.d.).
[33] I.E. Gordon, L.S. Rothman, R.J. Hargreaves, R. Hashemi, E.V. Karlovets, F. M. Skinner, E.K. Conway, C. Hill, R.V. Kochanov, Y. Tan, P. Wcisło, A.A. Finenko, K. Nelson, P.F. Bernath, M. Birk, V. Boudon, A. Campargue, K.V. Chance, A. Coustenis, B.J. Drouin, J.M. Flaud, R.R. Gamache, J.T. Hodges, D. Jacquemart, E.J. Mlawer, A.V. Nikitin, V.I. Perevalov, M. Rotger, J. Tennyson, G.C. Toon, H. Tran, V.G. Tyuterev, E.M. Adkins, A. Baker, A. Barbe, E. Canè, A.G. Császár, A. Dudaryonok, O. Egorov, A.J. Fleisher, H. Fleurbaey, A. Foltynowicz, T. Furtenbacher, J.J. Harrison, J.M. Hartmann, V.M. Horneman, X. Huang, T. Karman, J. Karns, S. Kassi, I. Kleiner, V. Kofman, F. Kwabia-Tchana, N. Lavrentieva, T.J. Lee, D.A. Long, A.A. Lukashevskaya, O.M. Lyulin, V. Y. Makhnev, W. Matt, S.T. Massie, M. Melosso, S.N. Mikhailenko, D. Mondelain, H. S.P. Müller, O.V. Naumenko, A. Perrin, O.L. Polyansky, E. Raddaoui, P.L. Raston, Z. D. Reed, M. Rey, C. Richard, R. Tóbiás, I. Sadiek, D.W. Schwenke, E. Starikova, K. Sung, F. Tamassia, S.A. Tashkun, J. Vander Auwera, I.A. Vasilenko, A.A. Vigasin, G.L. Villanueva, B. Vispoel, G. Wagner, A. Yachmenev, S.N. Yurchenko, The HITRAN2020 molecular spectroscopic database, J. Quant. Spectrosc. Radiat. Transf. 277 (2022).
[34] M. Giglio, P. Patimisco, A. Sampaolo, G. Scamarcio, F.K. Tittel, V. Spagnolo, Allan deviation plot as a tool for Quartz-enhanced photoacoustic sensors noise analysis, IEEE Trans. Ultrason. Ferroelectr. Freq. Control. 63 (2016) 555–560.